4-1-2014

Ordered Phases of Ethylene Adsorbed on Charged

Samuel Zottl
University of Innsbruck

Alexander Kaiser
University of Innsbruck

Matthias Daxner
University of Innsbruck

Marcelo Goulart
University of Innsbruck

Andreas Mauracher
University of Innsbruck

See next page for additional authors

Recommended Citation

S. Zöttl, A. Kaiser, M. Daxner, M. Goulart, A. Mauracher, M. Probst, F. Hagelberg, S. Denifl, P. Scheier, and O. Echt, Ordered Phases of Ethylene Adsorbed on Charged Fullerenes and their Aggregates Carbon 69 (2014) 206-220, DOI: 10.1016/j.carbon.2013.12.017, April 2014.

CARBON 69 (2014) 206–220

Available at www.sciencedirect.com

ScienceDirect

journal homepage: www.elsevier.com/locate/carbon

Ordered phases of ethylene adsorbed on charged fullerenes and their aggregates

Samuel Zöttl [a], Alexander Kaiser [a], Matthias Daxner [a], Marcelo Goulart [a], Andreas Mauracher [a], Michael Probst [a], Frank Hagelberg [b], Stephan Denifl [a], Paul Scheier [a,*], Olof Echt [a,c,*]

[a] Institut für Ionenphysik und Angewandte Physik, University of Innsbruck, Technikerstrasse 25, A-6020 Innsbruck, Austria
[b] Department of Physics and Astronomy, East Tennessee State University, Johnson City, TN 37614, USA
[c] Department of Physics, University of New Hampshire, Durham, NH 03824, USA

ARTICLE INFO

Article history:
Received 8 October 2013
Accepted 3 December 2013
Available online 12 December 2013

ABSTRACT

In spite of extensive investigations of ethylene adsorbed on graphite, bundles of nanotubes, and crystals of fullerenes, little is known about the existence of commensurate phases; they have escaped detection in almost all previous work. Here we present a combined experimental and theoretical study of ethylene adsorbed on free C_{60} and its aggregates. The ion yield of $(C_{60})_m(C_2H_4)_n^+$ measured by mass spectrometry reveals a propensity to form a structurally ordered phase on monomers, dimers and trimers of C_{60} in which all sterically accessible hollow sites over carbon rings are occupied. Presumably the enhancement of the corrugation by the curvature of the fullerene surface favors this phase which is akin to a hypothetical 1×1 phase on graphite. Experimental data also reveal the number of molecules in groove sites of the C_{60} dimer through tetramer. The identity of the sites, adsorption energies and orientations of the adsorbed molecules are determined by molecular dynamics calculations based on quantum chemical potentials, as well as density functional theory. The decrease in orientational order with increasing temperature is also explored in the simulations whereas in the experiment it is impossible to vary the temperature.

1. Introduction

The corrugation of the graphite surface has profound effects on the structure of adsorbates. Many electronically closed-shell atoms (He, Kr and Xe) and molecules (e.g., H_2, N_2, CO, CO_2, N_2O, CH_4) prefer hollow adsorption sites; for a certain range of coverage and temperature the adsorbate prefers the commensurate $\sqrt{3}\times\sqrt{3}$ phase in which one third of all hollow sites are occupied [1,2]. The distance between adsorbate molecules in this phase is $\sqrt{3}$ times the distance between adjacent hollow sites, or 4.26 Å. The coverage in this phase is 0.0637 molecules/Å^2 which is often referred to as a coverage $x = 1$ in dimensionless units; the average area occupied per molecule is 15.7 Å^2. For small atoms or molecules such as He or H_2 a coverage $x = 1$ does not yet complete a monolayer. Additional particles may be squeezed in resulting in loss of structural order or the formation of higher-order commensurate phases. However, the three times denser

* *Corresponding authors*. Address: Institut für Ionenphysik und Angewandte Physik, University of Innsbruck, Technikerstrasse 25, A-6020 Innsbruck, Austria. Fax: +1 603 862 2998.
E-mail addresses: paul.scheier@uibk.ac.at (P. Scheier), olof.echt@unh.edu (O. Echt).
0008-6223
http://dx.doi.org/10.1016/j.carbon.2013.12.017

1×1 phase (coverage $x = 3$), with all hollow sites occupied, does not form because the distance between adsorbate molecules would be 4.26 Å/$\sqrt{3}$ = 2.46 Å, significantly less than the size of any closed-shell atom or molecule.

For linear molecules the molecular orientation is another important factor because it controls the molecular size (projected onto the surface) as well as the interaction between neighbors. In general, individual molecules will prefer to lie flat on the graphitic surface and be orientationally ordered at low temperature [3]. Ethylene, a planar molecule, presents a particularly interesting case. Individual molecules on graphite lie flat with the C=C axis parallel to the surface but in this orientation ethylene is too large to form the $\sqrt{3} \times \sqrt{3}$ phase. At high coverage the C=C axis reorients perpendicular to the surface; its projected size is reduced. However, at low temperature its large anisotropy leads to orientational order which is inconsistent with the $\sqrt{3} \times \sqrt{3}$ structure which has one molecule per primitive unit cell.

The commensurate $\sqrt{3} \times \sqrt{3}$ phase may form at elevated temperature if the molecules rotate freely. However, this phase has escaped detection for a long time even though C_2H_4 monolayers on graphite were studied widely [4–8]; interesting features include a prewetting transition and what seemed to be a continuous melting transition [9–14]. In early work it was established that ethylene forms either a low-density (LD) phase in which the C=C axis of the molecules is parallel to the graphite surface, or a high-density (HD) phase in which the C=C axis is perpendicular. For intermediate coverage, $0.83 \leqslant x \leqslant 1.05$, the two phases co-exist. At temperatures exceeding about 35 K the molecules are orientationally disordered (D). These so-called DLD and DHD phases are triangular; the intermolecular spacings are 4.65 and 4.22 Å, i.e., either larger or smaller than 4.26 Å which is characteristic of the $\sqrt{3} \times \sqrt{3}$ lattice. The triangular phase may also be viewed as centered rectangular with a side ratio of 1:$\sqrt{3}$, i.e., the long side equals $\sqrt{3}$ times the intermolecular spacing; this centered rectangular cell comprises two primitive cells. Below about 35 K molecular rotation freezes resulting in the orientationally ordered (O) low density (OLD) and high density (OHD) phases. These phases are also centered rectangular but with a side ratio different from 1:$\sqrt{3}$; the rectangular cell comprises two inequivalent molecules which form a herringbone pattern.

The picture described above has emerged from neutron diffraction, NMR, X-ray, ellipsometry and heat capacity experiments. Molecular dynamics studies supported the idea that the corrugation of the graphite surface has a negligible effect on the structure of the ethylene adsorbate [7,13,15]. However, in 1991 Eden and Fain published low-energy electron diffraction data which revealed the existence of three additional solid phases at high temperatures [16,17]. One was observed when the low-density phase undergoes a transition from orientationally disordered incommensurate to orientationally disordered commensurate, although not to the commensurate $\sqrt{3} \times \sqrt{3}$ phase because the molecules are too large when they lie flat. Contrary to conclusions drawn in earlier work the authors argued that this phase melts discontinuously [16,17]. Two additional commensurate, orientationally disordered phases were identified by Eden and Fain at high density, with the molecules being in the T-shaped configuration [16,17]. One of them, the commensurate $\sqrt{3} \times \sqrt{3}$ phase, formed at temperatures above 58 K and densities $\approx 0.9 \leqslant x \leqslant \approx 1.03$. However, a possible problem with these measurements was the irreversible structural damage caused by the electron beam to the ethylene film within a matter of minutes.

Several later experimental and theoretical studies have been published which were devoted to ethylene adsorbed on graphite [14,18], bundles of nanotubes [19–23], or crystals of C_{60} [24]. Surprisingly, none addressed the possible existence of commensurate phases nor the orientation of the adsorbed molecules. In some of the theoretical work the corrugation of the substrate was entirely neglected [21]; in another study the six atoms in ethylene were represented by two pseudoatoms [23]. Other researchers [14,18] did not even mention the electron diffraction data by Eden and Fain. In short, detailed microscopic information on the ethylene–graphite system is still badly missing.

Here we present a combined experimental and theoretical study of ethylene adsorbed on positively charged aggregates of C_{60}. In some ways aggregates of C_{60} resemble bundles of nanotubes: they offer a curved, corrugated exterior surface and groove sites between pairs of C_{60}; they also offer sites in the dimples between adjacent C_{60}, similar to void sites in the strongly corrugated surface of a C_{60} crystal [24]. Which sites are most strongly bound? What are the adsorption capacities of these sites? Do commensurate phases form? Experiments involving bundles of nanotubes inevitably suffer from the non-uniformity of tubes and the presence of defects; these difficulties are avoided in the current experiments involving C_{60}. Also of interest are the differences between the surface of free fullerenes and planar graphite (or graphene) because the curvature of the substrate decreases the adsorption energies while it enhances the corrugation and increases the separation between adatoms at adjacent hollow sites [25,26].

Our experiment is based on a novel approach, namely synthesis of C_{60} aggregates inside nanometer-sized superfluid helium droplets; the aggregates are then exposed to ethylene and characterized by mass spectrometry. The ionization process causes partial dissociation of the C_{60}–ethylene complexes which leads to the enrichment of ions that are particularly stable. We are thus able to determine the adsorption capacities of distinct sites provided their adsorption energies differ. Several such sites are identified, namely registered sites that lead to a commensurate phase in which all hollow sites are occupied (the 1×1 phase), sites that correspond to completion of a monolayer, sites in the grooves between pairs of C_{60}, and dimple sites between triplets of C_{60} [27–31].

The identity of these sites, adsorption energies, and configurations of C_2H_4 in these sites are determined by molecular dynamics calculations based on quantum chemical potentials, as well as from optimizations based on density functional theory (DFT). The C_{60}–C_2H_4 interaction hypersurface was based on the ωB97X-D hybrid-functional which properly accounts for long-range dispersion forces. For the C_2H_4–C_2H_4 interactions previous CCSD(T) calculations which are even more accurate were augmented. In both cases, analytical all-atom pair potentials were fitted to the quantum chemical data. We also explored the effect of temperature in some of

the simulations in an effort to compensate for a characteristic feature of the experiment where the aggregates are isolated, hence their internal temperature cannot be varied nor can it be measured. Instead, the evaporative model is applied to estimate the relevant vibrational temperature [32–36].

2. Experimental

Neutral helium nanodroplets were produced by expanding helium (purity 99.9999%) from a stagnation pressure of 2 MPa through a 5 μm nozzle, cooled to about 9.5 K by a closed-cycle refrigerator (Sumitomo Heavy Industries LTD, model RDK-415D) into vacuum. The average number of helium atoms per droplet formed in the expansion ranges from 10^5 to 10^6; the droplets are superfluid with a temperature of ≈0.37 K [37]. The resulting supersonic beam was skimmed by a 0.8 mm conical skimmer, located 12 mm downstream from the nozzle. The skimmed beam traversed a differentially pumped pickup region into which a small amount of C_{60} (MER Corp., 99.9%) was vaporized from a crucible. The temperature, typically around 350 °C, was adjusted to either pick up just one fullerene per helium droplet, or to favor multiple pickup of fullerenes.

The doped helium droplets passed through a second, 20-cm long differentially pumped pickup region into which ethylene (Messer, purity 99.7%) was introduced. The measured partial pressure in the cell ranged from 1.5 to 3 mPa (uncorrected gauge signal).

After the pickup region the doped helium droplets passed a region in which they were ionized by electrons at 82 eV. It is worth mentioning that ionization introduces a substantial amount of excess energy into the aggregates; an estimate of their internal temperature will be provided in Section 4. Cations were accelerated to 40 eV into the extraction region of a commercial time-of-flight mass spectrometer equipped with a reflectron (Tofwerk AG, model HTOF); its mass resolution is about $\Delta m/m = 1/5000$. The base pressure in the mass spectrometer was 10^{-5} Pa. The ions were extracted at 90° into the field-free region of the spectrometer by a pulsed extraction voltage. At the end of the field-free region they entered a two-stage reflectron which reflects them towards a microchannel plate detector operated in single ion counting mode. Additional experimental details have been described elsewhere [38].

3. Theoretical methods

A combined quantum chemical (QC) and molecular dynamics (MD) approach was used to simulate and optimize complexes of C_2H_4 and C_{60}. We restricted our calculations to neutral complexes since we did not observe large differences between neutral and singly charged structures in our previous work on CH_4 adsorption on C_{60} [28,29]. We first calculated the potential energy surfaces (PES) for C_{60}–C_2H_4 and C_2H_4–C_2H_4 interaction and then fitted the PES by analytical pair potentials to obtain force fields for classical MD simulations.

Calculations with the long-range corrected density functional (ωB97X-D/6-31 g(d,p) [39–42]) provided the PES for C_{60}–C_2H_4 in a similar procedure as described in [29]. The ωB97X-D hybrid-functional is currently one of the best DFT functionals that properly describe long-range dispersion forces [43]. The PES was sampled by varying the position, orientation, and distance of C_2H_4 to the curved C_{60} surface. The ethylene-dimer PES had already been investigated with high-level theoretical methods by Kalugina et al. [44]. We used their extensive samples of CCSD(T)/aug-cc-pVTZ [45,46] energies that include the counterpoise correction for 12 different configurations. However, force fields fitted to these values resulted in wrong dimer geometries. Therefore we augmented their set of configurations by 179 additional random geometries. These geometries were constructed by placing the second C_2H_4 molecule in an arbitrary position with arbitrary orientation around the first C_2H_4 with the constraint that atoms were not allowed to overlap. By using this combined data set of potential energy scans in several directions and additional random configurations, a representative set of energies could be obtained while still keeping the possibility to visually examine the quality of the force fields for various analytical functions by inspecting a set of curves. Indeed we recommend this combined procedure, especially for molecules with strongly non-spherical symmetry. All random geometries and energies are given in the Supplementary material.

We fitted analytical all-atom pair potentials to the PES for both C_{60}–C_2H_4 and C_2H_4–C_2H_4. Fitting the C_{60}–C_2H_4 interactions was straightforward using Lennard–Jones potentials of the 10–8 type. The C_2H_4–C_2H_4 force field first eluded high quality fitting completely even when additional point charges were used to mimic quadrupole interactions. One atomic charge parameter (q_C; $q_H = -q_C/2$) was also a fitting parameter. Our best results were finally obtained using analytical functions with two repulsive and two attractive C_j/r^j terms in addition to the Coulomb interactions. With these functions we achieved a root mean square (*rms*) deviation of 8 meV that is better than the *rms* deviation of 12.8 meV of a standard OPLS-AA parameter set [47] to the CCSD(T) energies. Furthermore, our force field gives the correct optimized dimer geometry and binding energy which we discuss in detail in Section 5.1. After an extensive search through potential energy terms of Lennard–Jones, Buckingham, Born–Huggins–Meyer, and Morse type and combinations thereof we conclude that the C_2H_4 dimer PES cannot be fitted perfectly using only pair potentials. The C_{60}–C_{60} interaction was modeled by the 12–6 Lennard–Jones potential of Girifalco and Lad [48]. All parameters and analytical formulas of the force fields are given in the Supplementary material together with single point energies for certain structures to provide a proper testing procedure.

With these force fields clusters of rigid C_2H_4 and rigid C_{60} molecules were simulated by classical MD. The initial structures were generated by placing C_2H_4 molecules one at a time around optimized C_{60} aggregates at random positions and orientations with the constraint not to overlap with any other atoms of the system. This procedure gives a diffuse cloud of C_2H_4 molecules that surrounds C_{60} aggregates. Temperature was controlled in NVT ensemble with a Nosé–Hoover thermostat [49,50] with a relaxation time of 0.5 ps. All structures were given enough time for relaxation (>20 ps depending on the system size) before starting production runs. During the

relaxation process the whole ensemble was annealed in 4 steps from starting temperatures between 40 and 100 K towards the production temperature of 4 K that was also used in [29]. For comparison with standard force fields we have redone some simulations using OPLS-AA parameters [47,51] in the DL_POLY_2 program [52] with frozen C_{60} at optimized geometries. We observed only small changes in the number of molecules in the grooves and first shells. We also compared using frozen and non-frozen C_{60} clusters with our new force field and got very similar results. This confirms our previous conclusion [28,29] that C_{60} dynamics do not alter the structure of the adsorbents much if the adsorbent-C_{60} interaction is smaller than the C_{60}–C_{60} interaction.

The simulations were performed with our own code which supports the use of arbitrary analytical functions as force fields and is specially tailored for simulation and energy minimization of clusters in vacuum without boundary conditions. In our current experimental version we used the simple ode45 integrator of MATLAB with variable time-stepping. We are currently developing a symplectic method with constant time-steps and better scaling. The estimates for the global energy minima were obtained from simulated annealing followed by an optimization with analytical gradients using a subspace trust-region method [53].

Clusters of C_{60} and C_2H_4 were optimized by temperature annealing to zero kelvin followed by global optimization. Several strategies of annealing involving different equilibration processes and starting temperatures between 40 and 100 K as well as different simulation lengths were used. We also tried heating followed by annealing and optimization. Several runs (up to 5) ensured that good estimates for the global energy-minimum were reached. We also re-optimized some important clusters using plane wave-density functional theory (PL-DFT) as implemented in the code Vasp 5.2 [54] and PAW-PBE potentials [55,56], supplemented by the long-range correction proposed by Grimme [39]. There a plane wave cutoff of 500 eV was chosen and periodic boundary conditions were employed, with a large unit cell (40 Å) to simulate the clusters in vacuum.

4. Experimental results

Sections of a representative mass spectrum of helium droplets doped with C_{60} and ethylene (Et) are shown in Fig. 1 on a semi-logarithmic scale. The spectrum was recorded with a helium pressure of 2 MPa and nozzle temperature of 9.55 K; the estimated average size of the helium droplets was a few times 10^5 [37]. The temperature of the C_{60} cell was 620 K; the C_2H_4 pressure was 2.8 mPa (uncorrected ion gauge signal).

The most prominent ions in Fig. 1, $(C_{60})_m^+$, $m = 1, 2, 3$, are labeled. Each of these ions gives rise to a group of resolved mass peaks that differ in the number of ^{13}C isotopes; isotopically pure ions, $(^{12}C_{60})_m^+$, are flagged. The relative intensities of the first few peaks in each group follow the pattern calculated from the natural abundance of ^{13}C (1.07%). We conclude that no other ions, such as $(C_{60})_mH^+$, contribute significantly to these mass peaks.

Also marked in Fig. 1 are isotopically pure $(C_{60})_mEt_n^+$. For small n the relative intensities of the peaks in each group

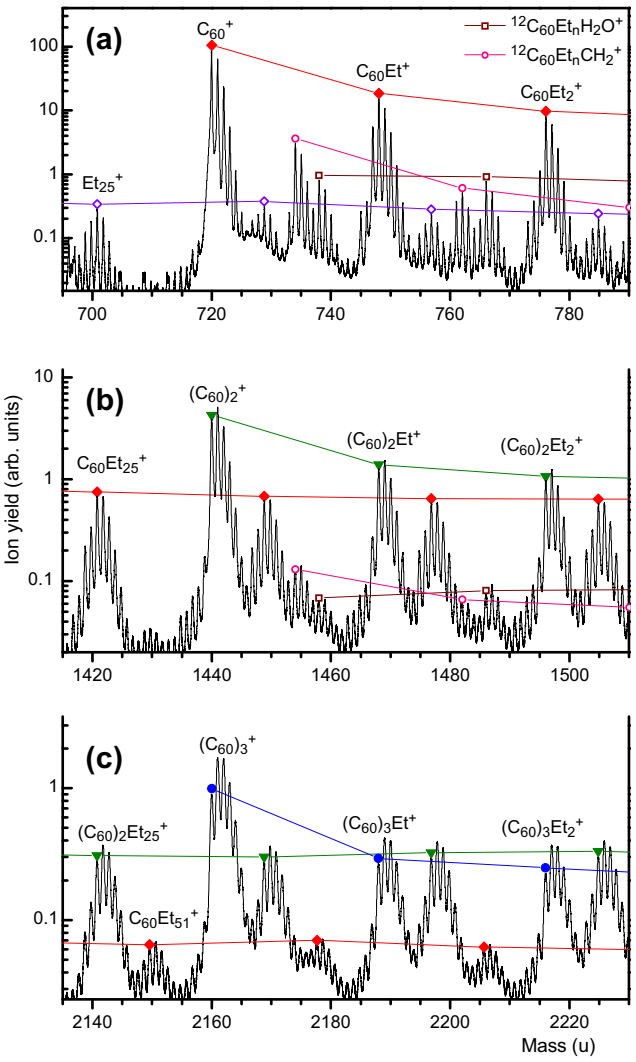

Fig. 1 – Mass spectrum of helium nanodroplets doped with C_{60} and ethylene (Et). Shown are the mass regions around the bare C_{60} monomer through trimer (panels a through c). The most prominent ion series are due to $(C_{60})_mEt_n^+$ ($m = 0, 1, 2, 3$). Each of these ions forms a group of mass peaks that differ in the number of ^{13}C (natural abundance 1.07%). Ions that contain no ^{13}C are marked by symbols; ions belonging to the same series (same value of m) are connected by lines. Also marked in panels a and b are isotopically pure ions (no. ^{13}C) that contain a water impurity or a CH_2 unit (open symbols). (A colour version of this figure can be viewed online.)

follow the expected pattern of isotopologues; this implies that ion–molecule reactions which conceivably could lead to protonated or dehydrogenated ions, $(C_{60})_mEt_{n-1}C_2H_5^+$ or $(C_{60})_mEt_{n-1}C_2H_3^+$, do not play a major role. The agreement between the observed and expected patterns is less convincing for large values of n. For example, the first group of mass peaks in each panel of Fig. 1 is due to $(C_{60})_mEt_{25}^+$ with $m = 0, 1, 2$, respectively. These ions have just 10 fewer carbon atoms than the next group, $(C_{60})_m^+$ with $m = 1, 2, 3$, respectively. In the absence of ion–molecule reactions the patterns would be quite similar, but they are not. Most noticeable is the occurrence of peaks

at 1 u below the ones that are marked, i.e., 1 u below the isotopically pure $(C_{60})_mEt_n^+$. These additional peaks are probably due to dehydrogenated ions.

Two other ion series are marked in panels a and b of Fig. 1, namely isotopically pure $(C_{60})_mEt_nH_2O^+$ and $(C_{60})_mEt_nCH_2^+$. The first one is obviously due to H_2O pickup by helium droplets, the second one probably due to C=C bond breakage upon ionization. However, the NIST spectrum of ethylene shows only a very minor (2%) yield for CH_2^+ [57] and our data show only minor production of $Et_nCH_2^+$ upon ionization of pure ethylene clusters. Anyhow, the yield of ions containing H_2O or CH_2 is less than 10% of the ions of main interest, $(C_{60})_mEt_n^+$.

An extended range of the mass spectrum discussed above is displayed in Fig. 2. Individual mass peaks within each group are no longer discernible. The most prominent ion series are $(C_{60})_mEt_n^+$ (m = 1, 2, 3, 4). Here we marked the isotopologues that are the most or second most abundant, i.e., the ones that contain one ^{13}C in panels a and b, and two ^{13}C in panel c. For most parts the ion yield within a series (fixed m) varies smoothly with n but there are noticeable exceptions where the yield changes abruptly; the corresponding values of (m, n) are indicated.

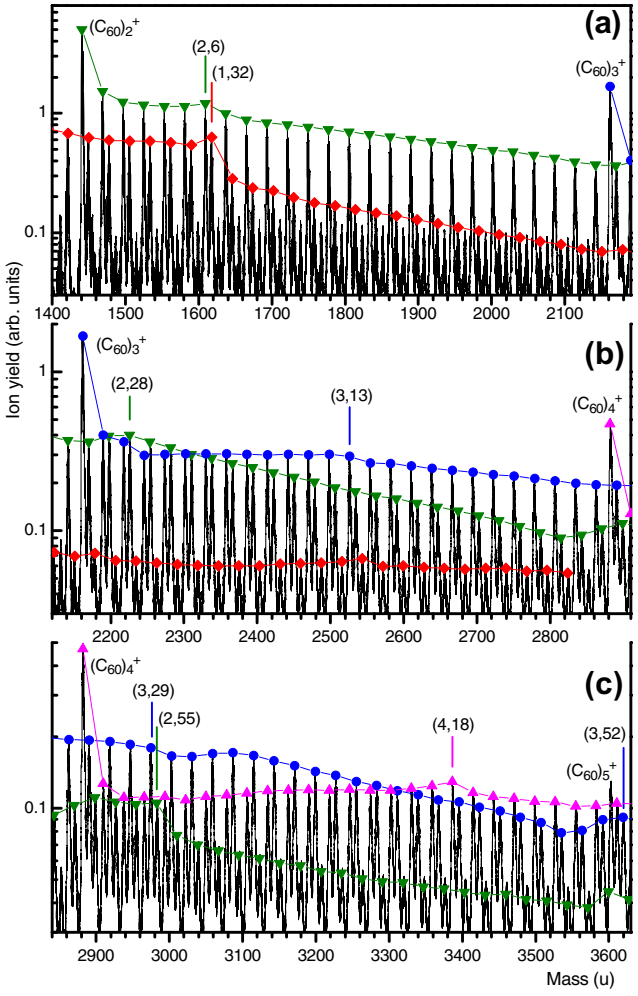

Fig. 2 – Mass spectrum of helium nanodroplets doped with C_{60} and ethylene (Et), displayed in three overlapping sections from 1400 to 3630 u. For each $(C_{60})_mEt_n^+$ ion the most abundant isotopologue is marked, ions with the same value of m are connected by lines. Several significant anomalies in the ion yield *versus* n are observed; the corresponding (m, n) values are indicated. (A colour version of this figure can be viewed online.)

Fig. 3 provides a clearer view of the ion yield of $(C_{60})_mEt_n^+$ *versus* n for m = 1, 2, 3, 4. The yield is shown for the isotopologues that are the most or second most abundant. Anomalies in the distributions that are deemed significant are indicated, and compiled in Table 1. The criterion is that the anomaly occurs for all isotopologues that have a significant yield. The spectra have been visually inspected to rule out artifacts, such as traces of C_{70} impurities in the fullerene sample.

In principle, anomalies in the ion yield I_n of clusters may be caused by several factors including kinetics, size-selective ionization, or anomalies in the microcanonical heat capacities. For atomic clusters that are prone to fragmentation upon ionization the usual cause [58–60] are anomalies in the adsorption energies D_n, i.e., the energy of the reaction:

$$(C_{60})_mEt_n \rightarrow (C_{60})_mEt_{n-1} + Et - D_n \quad (1)$$

With this definition D_n is positive; it equals the energy needed to adiabatically remove the least-bound molecule adsorbed on $(C_{60})_mEt_n^+$. Other frequently encountered names for D_n are dissociation, evaporation, desorption or separation energy.

The quantitative relation between the size dependence of D_n and I_n has been explored by several authors [33,35,36] based on the model of the evaporative ensemble [32]. Key

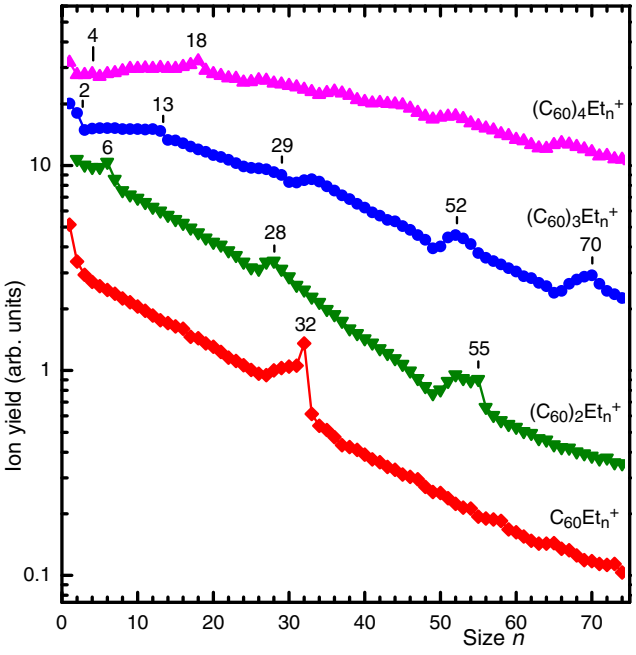

Fig. 3 – Ion yield of C_{60}–ethylene complexes containing up to 4 C_{60} plotted *versus* the number n of adsorbed C_2H_4. Significant anomalies are marked; they indicate enhanced adsorption energies. (A colour version of this figure can be viewed online.)

Table 1 – Anomalies observed in the ion yield of $(C_{60})_mEt_n$ together with the numbers n of ethylene molecules in specific adsorption sites, extracted from computed spatial distributions.

C_{60} aggregate	n (Exp)	Theory (neutral aggregates)		
		Dimple	Groove	Full layer
C_{60}^+	32	N/A	N/A	32
$(C_{60})_2^+$	6, 28, 55	N/A	6	56–58
$(C_{60})_3^+$	2, 13, 29, 52?, 70	2	13	70–75
$(C_{60})_4^+$	4?, 18	4	18	

ingredients of this model are that the initial cluster distribution is broad, dissociation is a statistical process, and each cluster ion that is observed has undergone at least one evaporation. These assumptions are met in our case. In particular, growth of clusters in helium nanodroplets by pickup of individual constituents is a statistical process [37], the ensuing cluster size distributions are featureless, and anomalies in the distributions of cluster ions provide evidence for ionization-induced dissociation, i.e., loss of adsorbate molecules. The small heat capacity of clusters containing less than $n \approx 10^2$ units ensures that each evaporation cools the cluster significantly, thus leading to a drastic (at least a factor 10) reduction of the dissociation rate coefficient. In the limiting case of extremely small heat capacities I_n will be, on a local scale, proportional to D_n [27,34,61], but the rotational degrees of freedom of C_2H_4 probably imply that this limit is not reached in the present work. Still, it is reasonable to interpret an abrupt drop in the ion yield between $(C_{60})_mEt_n^+$ and $(C_{60})_mEt_{n+1}^+$ as a sign that $(C_{60})_mEt_n^+$ features relatively high stability, usually caused by completion of a solvation shell, a subshell, or a commensurate layer.

The internal temperature T of the aggregates is another important quantity in the interpretation of the experimental results. T cannot be controlled in our experiment but it may be estimated from the computed adsorption energies D_n by applying the concept of the evaporative ensemble [32,62]. As noted above, anomalies in the ion yield of cluster ions result from dissociation, i.e., desorption of adsorbate molecules. Ionization of doped helium droplets by electrons involves formation of He^+, followed by resonant charge transfer between helium atoms, and ending with charge transfer from He^+ to the dopant [63]. This latter step releases about 17 eV, the difference between the ionization energies of He and C_{60}. As a result, a large number of adsorbate molecules, in addition to He, will be ejected from the nascent ion. Approximately 2 ms elapse between ionization and mass spectral analysis; during this time t the highly excited droplets will cool by desorption until the rate coefficient k equals approximately $1/t$, i.e., $k \approx 500\ s^{-1}$. k strongly depends on the vibrational temperature T and the adsorption energy D_n; hence T may be estimated from k and D_n. Without going into details, k_BT (where k_B = Boltzmann constant) will approximately equal D_n divided by the Gspann factor which equals about 25 [32,61,64].

Our calculations to be discussed below provide a value of $D_{32} = 239$ meV for the adiabatic adsorption energy of $C_{60}Et_{32}$, thus the estimated vibrational temperature of $C_{60}Et_{32}^+$ in the experiment is 110 K.

5. Theoretical results and discussion

5.1. *Pure C_{60} aggregates and C_2H_4 clusters*

Before discussing adsorption of C_2H_4 on C_{60} aggregates, pure C_{60} and pure C_2H_4 clusters deserve some attention since these results test the quality of the force fields. Dissociation energies and geometries for neutral C_{60} dimer to pentamer are given in Table 2. In analogy with Eq. (1), the dissociation energy $D_{C60,m}$ of $(C_{60})_m$ is the energy of the reaction

$$(C_{60})_m \rightarrow (C_{60})_{m-1} + C_{60} - D_{C60,m} \quad (2)$$

$D_{C60,m}$ describes the energy needed to adiabatically remove the least-bound C_{60} from $(C_{60})_m$. The C_{60}-dimer dissociation energy of 257 meV from classical optimization with the Girifalco potential [48] is confirmed by re-optimization with PL-DFT giving 250 meV which compares well with an experimental value of 275 ± 80 meV [65] and is of the same order of magnitude as the energy of 410 meV of our DFT-optimized (ωB97X-D/6-31 g(d,p)) dimer using Gaussian 09. For our purpose more important is the excellent agreement in the C_{60} dimer distance of $d_{C60} = 9.81$ Å (measured center to center) with the DFT value of 9.83 Å. Tournus et al. [66] calculated a binding energy of 166 meV and a distance of 9.84 Å for the H-HH orientation, where a hexagon (H) faces a bond between two hexagons (HH). Our MD-optimized structure is similar to the DFT-optimized dimer shown in Fig. 7 of [29]. Zettergren et al. [67] studied neutral and charged C_{60} dimers using the BLYP functional with an empirical long-range correction and obtained $D_{C60,2} = 336$ meV.

The dissociation energy of the trimer is, as expected, almost twice the dimer value because the additional C_{60} interacts with two C_{60} at almost the same distance, $d_{C60} = 9.85$ Å (for the trimer and larger aggregates d_{C60} represents the average of all nearest-neighbor distances). We have also studied the neutral C_{60} trimer with PL-DFT. We obtained a structure where the hexagons approximately point to the center of the trimer and $d_{C60} = 10.42$ Å. The PL-DFT dissociation energy $D_{C60,3} = 362$ meV is smaller than our MD value of 497 meV, and at the same time smaller than the value of the dimer DFT calculations (410 meV) with ωB97X-D.

$D_{C60,4}$ equals almost 3 $D_{C60,2}$ since in the tetrahedral structure each C_{60} interacts with three C_{60}. Five C_{60} form a square pyramid in which each base molecule has only three nearest neighbors, therefore $D_{C60,5}$ is only slightly larger than $D_{C60,4}$. All multimer structures agree well with optimizations from Doye and Wales [68] based on the potential of Pacheco and Prates-Ramalho [69]. Our C_{60}–C_{60} distances are slightly

Table 2 – Dissociation energies $D_{C60,m}$ and average nearest-neighbor distances d_{C60} (center-to-center) for neutral $(C_{60})_m$ calculated with the Girifalco potential [48]. The minimum energy structure of $(C_{60})_5$ is a square pyramid.

C_{60} aggregate	$D_{C60,m}$ (meV)	d_{C60} (Å)
$(C_{60})_2$	257	9.81
$(C_{60})_3$	497	9.85
$(C_{60})_4$	718	9.88
$(C_{60})_5$	735	9.89

smaller though, i.e., 9.85 Å compared to 10.02 Å for the trimer. Overall the Girifalco potential used in this work for C_{60}–C_{60} interaction seems slightly too shallow but it gives very good geometries and reasonable relative dissociation energies.

Pure $(Et)_n$ clusters up to $n = 25$ were already studied by Takeuchi using classical potentials based on MP2 data to optimize geometries [70]. Although we cannot be sure that we have reached global minima especially for large n our cluster energies agree for $n = 2$ to 25 within 10% except for $n = 2$ (10.4%), and $n = 4$ (14.5%) using only 6 different initial geometries compared to 200–50,000 considered by Takeuchi. In fact, all our energies are deeper, most of them 5–10%. For our force field the dimer structure is the exact *T-shape* or *cross form* as displayed in [70] with a binding energy of 57.2 meV and not Takeuchi's slightly tilted also T-shaped *global-minimum form* that has a binding energy of 51.2 meV. The cross form with D_{2d} symmetry that we obtained was also found experimentally by Chan et al. using near-infrared spectroscopy [71] and recently confirmed by Rezaei et al. [72]. Rezaei et al. determined an inter-molecular separation of 3.867 Å which agrees reasonably well with our calculated value of 3.71 Å. Our dimer results can also be compared with ab initio data by Kalugina et al. [44] that were also used for force field fitting. Their optimized configuration was T-shaped (D_{2d}) as well with an equilibrium distance of 3.8 Å and a binding energy of 59.6 meV. Tascon and Bottani used a force field with 27.5 meV binding energy at 3.88 Å [24]. We re-optimized the MD structure of the dimer with PL-DFT and got a binding energy of 85 meV that is 48% larger than our MD-value. The trimer geometry is similar to the geometry calculated by Takeuchi [70] that was confirmed experimentally by Rezaei et al. [72]; however our force fields yield a larger tilt angle. Overall we are confident that our force field for Et–Et interaction is well suited for the purposes of this research project.

5.2. *Adsorption of a single C_2H_4 on C_{60} and its aggregates*

Next we consider the adsorption energies D_1 of a single ethylene molecule adsorbed on $(C_{60})_m$. We have considered various adsorption sites and optimized the structures. The most favorable adsorption site on C_{60} is at the center of a carbon hexagon, with $D_1 = 161$ meV and a distance of $d_{Et} = 6.588$ Å. The complex is displayed in Fig. 4 a and b; numerical values are listed in Table 3. We will call this configuration the *simple hollow site*. D_1 decreases to 147 meV for adsorption at a pentagonal site. In relative terms the same decrease by about 10% between the two different sites was found for adsorption of He [27] and CH_4 [28,29]. For H_2 adsorbed on C_{60}^+, however, the difference was about 20% [30]. Due to the curvature of C_{60} it is to be expected that our adsorption energy of 161 meV lies below the value on graphite. The calculated isosteric heat of adsorption of 191.9 meV on graphite [73] and adsorption energies of 209.9 or 181.7 meV calculated with two different potentials [74] agree well with the experimentally determined isosteric heat of adsorption of 211 ± 2 meV extrapolated to zero coverage [6]. A re-optimization of our MD structure with PL-DFT leads to a rather small adsorption energy of 108 meV.

As shown in Fig. 4 a and b the C=C axis of the ethylene molecule lies flat against the fullerene face; the valence angle α which measures the orientation of the C=C axis with respect to the fullerene face equals 90°. α is defined by three points, the center of mass (COM) of C_{60}, the COM of C_2H_4, and a carbon atom of C_2H_4. For $\alpha = 90°$ the C=C axis is tangentially oriented; for 0° it would be radially oriented. However, the ethylene plane is not parallel to the fullerene face but shows a tilt. To quantify the tilt we measure the dihedral angle β defined by four points: The COM of C_{60}, the COM of C_2H_4, a carbon and a hydrogen atom of C_2H_4. This definition gives $\beta = 90°$ if ethylene lies flat on the fullerene face. The optimized C_{60}Et structure with Et above the hexagon shows a tilt $\beta = 71°$, see Fig. 4b. Klein and coworkers [13,15] also reported substantial tilts for ethylene adsorbed on graphite, but here the tilt arose from the interaction among the adsorbed molecules.

For fullerene dimers ethylene preferentially adsorbs in the groove with an adsorption energy $D_1 = 310$ meV, almost twice the value of the simple hollow site. For comparison, Rawat and Migone [22] measured 243 ± 10 meV for the isosteric heats of adsorption for ethylene in nanotube grooves. Approximately 190 meV were obtained by Cruz and Mota in a Monte Carlo calculation for bundles of nanotubes of 11 Å diameter at zero loading [19]; this value is probably too low because it barely exceeds the reported adsorption energies on graphite. The re-optimization of our MD-structure with PL-DFT yields an adsorption energy of only 171 meV in the groove which is also rather small because the Et–C_{60} (108 meV) interaction is already weak. On the other side the Et–C_{60} interaction in our MD simulation might be slightly too strong because the dispersion correction of ωB97X-D often overshoots [75,76]. The MD-optimized $(C_{60})_2$Et geometry is presented in Fig. 4c. The C=C axis lies tangentially in the groove; the C_{60} dimer axis is normal to the C_2H_4 plane. We call it *wedge* geometry. The distance to the nearest C_{60}, $d_{Et} = 6.69$ Å, is slightly larger than for the simple hollow site.

The dimple site in the trimer offers, with $D_1 = 413$ meV, almost three times the adsorption energy of a simple hollow site at a distance $d_{Et} = 6.689$ Å. The geometry is depicted in Fig. 4d. The C=C axis is approximately tangential to one of the grooves while one of the H-atoms dives into the dimple site. Adsorption energies of 400 meV in dimple sites of C_{60} tetramers and pentamers are almost as favorable as in the trimer. The reason for the small decrease could be related to the fact that the mean nearest neighbor distance between C_{60} molecules increases slightly from 9.88 Å for the trimer to 9.9 Å for the tetramer and pentamer. The tetramer may be seen as a trimer with an additional C_{60} in its dimple site that is, however, far too large for a proper fit; this increases the inter-C_{60} separation.

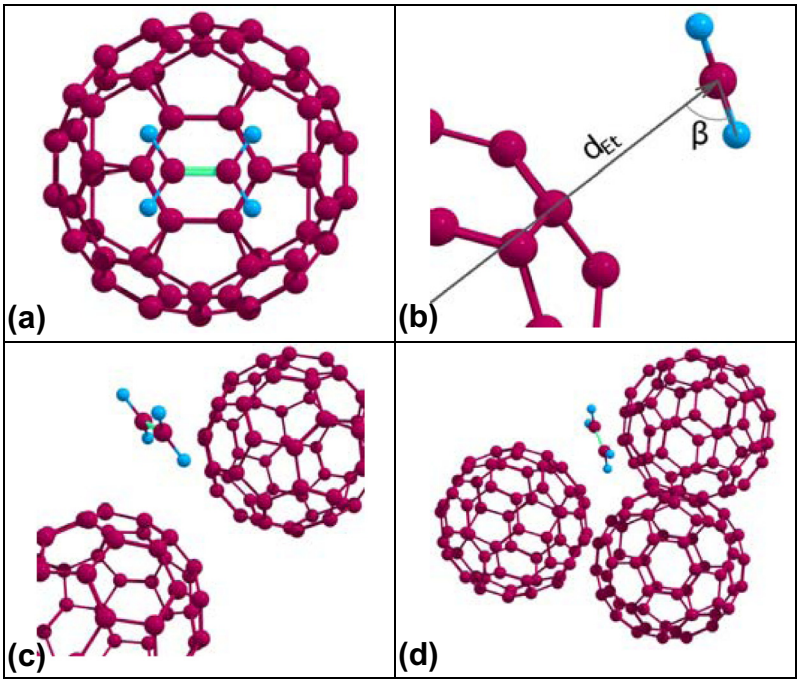

Fig. 4 – MD optimized structures of a hollow site in $C_{60}C_2H_4$ in top view (a) and side view (b), a groove site in $(C_{60})_2C_2H_4$ (c) and a dimple site in $(C60)_3C_2H_4$. The tilt angle β is shown together with the definition of the Et–C_{60} distance d_{Et} in panel b.

Table 3 – Calculated adsorption energies D_1 of a single C_2H_4 adsorbed on neutral C_{60} aggregates at various sites. Also listed are the average distances d_{Et} of C_2H_4 to the nearest fullerene(s) and the average nearest-neighbor distances d_{C60} between fullerenes.

C_{60} aggregate	Position of C_2H_4	D_1 (meV)	d_{Et} (Å)	d_{C60} (Å)
C_{60}	Hexagon	161	6.588	N/A
C_{60}	Pentagon	147	6.706	N/A
$(C_{60})_2$	Groove	310	6.689	9.82
$(C_{60})_3$	Dimple	413	6.898	9.88
$(C_{60})_4$	Dimple	400	6.936	9.9
$(C_{60})_5$	Dimple	400	6.934	9.9

5.3. *Adsorption capacities of specific sites and comparison with experiment*

One goal of the present work is to determine the nature and storage capacity of specific adsorption sites of fullerene–ethylene complexes by combining experiment and theory. The experiment, which refers to $(C_{60})_mEt_n^+$ ions, provides us with a set of numbers n for $m = 1$ through 4 which are listed in Table 1. These numbers indicate enhanced stability of $(C_{60})_mEt_n^+$ relative to the next larger or smaller complex. The enhancement is quite dramatic for $C_{60}Et_{32}^+$, see Fig. 3. It is customary to refer to these n- values as "magic numbers" [58,60] even if the complex is not more stable than the next smaller one (such as $(C_{60})_2Et_{55}^+$ or if the enhancement is small.

The "magic numbers" provide a stringent test to theory which, ideally, would compute the energies of all complexes in their ground state configurations in order to determine the adiabatic adsorption energies D_n defined in Eq. (1). We have used this approach in a previous study of $C_{60}He_n^+$ [27] but given the importance of the molecular orientation this approach would be prohibitively time consuming in the present case. Therefore we resort to an approach adopted in a recent study of $(C_{60})_m(CH_4)_n$ [28,29]: For each value of m, values of n, larger than any magic number to be interpreted, are chosen. In this work $(C_{60})_mEt_n$ complexes with $n = 50$, 100, 200, 300 and 500 were chosen. Simulated annealing in MD-simulations starting from several different random initial geometries is then performed down to a small temperature, where the clusters are near their ground state geometry. The exact procedure was described in Section 3. With suitable definitions discussed below we can then determine the number of molecules in the first adsorption layer, in groove sites, and in dimple sites.

Concerning the energetics, we calculate the energy E_x $(1 \leqslant x \leqslant n)$ for each molecule in the complex where E_x is defined as the sum over all pairwise interactions with the fullerenes and all other C_2H_4 in the complex. E_x is negative; the most strongly bound molecules will have the lowest (most

negative) value. $-E_x$ equals the vertical desorption energy of molecule x from $(C_{60})_mEt_n$.

Some results of this analysis are presented in Fig. 5. We only show a few of our results that display the shell structure particularly well. Panel a displays the cumulative sum of molecules *versus* their distance from the center of the nearest fullerene which we call min{d_i}, the minimum of distances d_i from all fullerenes in the complex. The cumulative sum is shown rather than a histogram because it avoids clutter. One sees very distinct plateaus, which correspond to gaps in the histograms, when the first adsorption layer is filled at

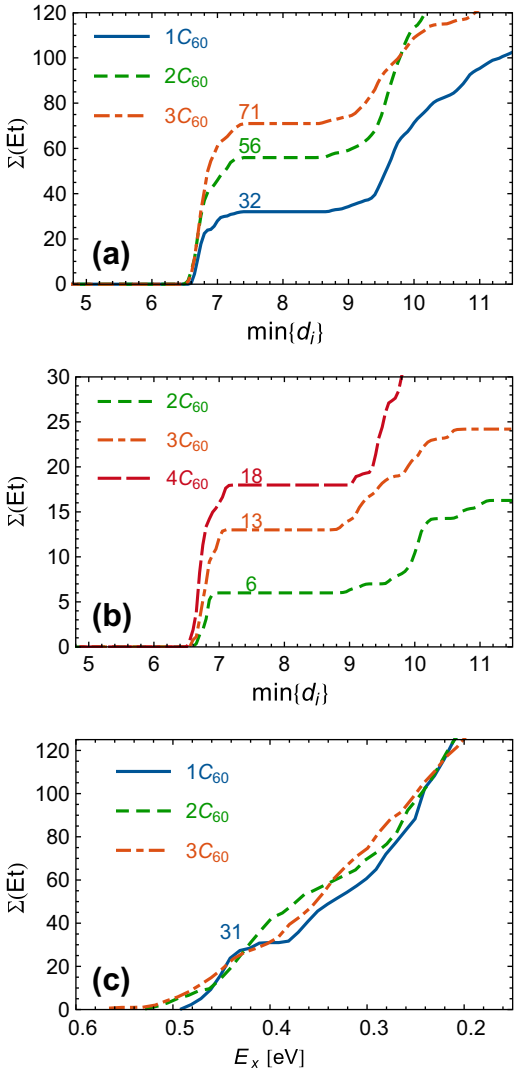

Fig. 5 – Panel a: The cumulative sums of ethylene molecules *versus* their distance min{d_i} from the nearest C_{60} for the monomer, dimer, and trimer. Plateaus signal completion of the first adsorption layer. Panel b: The cumulative sums of molecules that lie in the midplane between any pair of fullerenes; plateaus indicate completion of groove sites for the dimer through tetramer. Panel c: The cumulative sums of molecules *versus* their energy E in the complex, computed as the sum of pairwise interactions (see text for details). A clear plateau is seen only for the C_{60} monomer. (A colour version of this figure can be viewed online.)

$n = 32$ for C_{60}, 56 for $(C_{60})_2$, and 71 for $(C_{60})_3$. The flatness and width of the plateaus indicate spatially distinct first and second adsorption layers; no molecules reside at a radial distance of ≈8 Å.

For the monomer the agreement with experiment is perfect. Further analysis of the 32 molecules in the first layer shows that, as expected, all molecules reside near the centers of the 32 (20 hexagonal plus 12 pentagonal) hollow sites, in agreement with our findings for C_{60}-helium and C_{60}-methane [27–29]. The 32 innermost ethylene molecules form a commensurate phase which we call the 1×1 phase because all hollow sites are occupied. The orientational order of the molecules in this phase and its temperature dependence will be discussed in Section 5.4.

For the C_{60} dimer and trimer the calculated number of molecules in the first layer varies slightly from run to run because annealing does not always result in the ground state configuration. The numbers in the first layer range from $n = 56$ to 58 for the C_{60} dimer and from 70 to 75 for the trimer, see Table 1, in fair agreement with the experimental magic number $n = 55$ for the dimer (which features an abrupt drop in the ion yield, see Fig. 3) and 70 for the trimer (which features a broad local maximum). The simulations reveal that the molecules have a clear preference to occupy all sterically accessible hollow sites, and the 1×1 commensurate phase completes the first adsorption layer which, according to a simple model discussed below, would comprise $n = 56$ molecules for $(C_{60})_2$.

Fig. 5b shows the cumulative sum of molecules that reside in the groove regions of the C_{60} dimer, trimer and tetramer or, in other words, near the midplane between any pair of adjacent C_{60}. These data are derived similarly to those in Fig. 5a but only counting molecules for which the two shortest distances d_i to the centers of fullerenes are equal within 1 Å (see [29] for additional details). The plateaus occur at $n = 6$, 13, and 18 for the C_{60} dimer through tetramer, in exact agreement with the observed magic numbers. Furthermore, the plateaus are flat and wide, and the same values are obtained in most runs. They differ slightly from the values $n = 7$, 13 and 16 observed for C_{60}–methane complexes [29]; $n = 7$ was also observed for nitrogen and oxygen adsorbed on C_{60} dimers [31]. C_2H_4 is a slightly larger molecule than CH_4, O_2 and N_2, especially if it lies flat, thus it is not surprising that slightly fewer C_2H_4 fit into groove sites. However, it is worth mentioning that $(C_{60})_2(CH_4)_n^+$ also seems to prefer 6 molecules in the groove if properly annealed [29].

With 6 C_2H_4 residing in groove sites of $(C_{60})_2$ a simple geometric model predicts a total of 56 molecules in the first adsorption layer: The fullerene dimer has, essentially, two abutting hexagonal faces that are nearly parallel [29]. Thus, 2 of the 64 hollow sites of the 2 fullerenes are inaccessible. Each fullerene offers six hollow sites in the wedge of the dimer. In other words, each of the 6 molecules in the groove are wedged between two hollow sites. That leaves another 50 (=64−2−12) regular, external hollow sites, for a total of $n = 56$ in the first complete, commensurate adsorption layer of $(C_{60})_2$. This magic number is, indeed, observed for $(C_{60})_2$–methane, but for $(C_{60})_2$–ethylene we observe $n = 55$.

Fig. 5c displays the cumulative sum of molecules with energies less than E. Only for the monomer does one observe

a well-defined plateau although, surprisingly, at $n = 31$ rather than 32.

The absence of plateaus for the C_{60} dimer and trimer, expected at $n \approx 56$ and ≈ 71, is surprising, given the distinct spatial shell structure seen in Fig. 5a. In our previous study of C_{60}–CH_4 we found good agreement between spatial and energetic shells. Perhaps the large anisotropy of C_2H_4 makes it difficult to find true ground state configurations, leading to large errors in the energies. The limited degree of orientational order, to be discussed in Section 5.4, will compound the problem. Furthermore, it is conceivable that, due to the anisotropy, vertical desorption energies that we actually calculate are unreliable predictors of adiabatic adsorption energies that affect the experimental ion yield.

To further explore this issue we have computed adiabatic adsorption energies D_n (defined in Eq. (1)) for $(C_{60})_2Et_n$ with $1 \leqslant n \leqslant 10$ and $(C_{60})_3Et_n$ with $11 \leqslant n \leqslant 14$. Results are displayed in Fig. 6. According to experiment (Fig. 3) and calculated spatial distributions (Fig. 5b), groove sites are completely filled at $n = 6$ (dimer) and 13 (trimer). The MD-values (blue, dashed curves) show, indeed, a clear decrease in adsorption energies after the magic numbers 6 and 13 (another drop in D_n is seen for the C_{60} trimer from $n = 11$ to 12 which does not appear in the experiment). The PL-DFT values would suggest magic numbers that are spread out, namely at 5 and 6 for the C_{60} dimer and at 12 and 13 for the trimer. This is not supported by

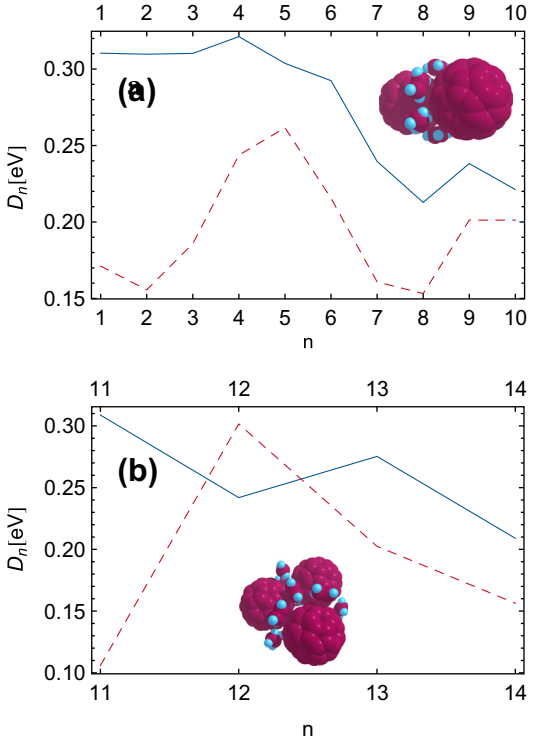

Fig. 6 – Adiabatic adsorption energies D_n of ethylene for the dimer (upper panel) and trimer (lower panel) *versus* the total number *n* of adsorbed molecules. Blue solid curves represent MD-values and red dashed curves re-optimized PL-DFT values. Abrupt drops in D_n occur when all groove sites are filled. (A colour version of this figure can be viewed online.)

the experimental data (Fig. 3). If anything, a consecutive drop in D_n occurs for the C_{60} dimer from $n = 6$ to 7 and 7 to 8.

For smaller values of *n* the MD and PL-DFT values disagree significantly; the latter are much smaller than the former. The origin of this difference could be the large difference in relative dissociation energies of C_{60}–Et compared to Et–Et. The classical C_{60}–Et interaction of 161 meV is 2.81 times as strong as the Et–Et interaction (57.2 meV) while for PL-DFT the factor is only 1.27. Therefore in MD the presence of other molecules in the groove is less important than for PL-DFT. Consequently, in the classical simulations all ethylene molecules in groove sites have about the same adsorption energies while for PL-DFT the adsorption energies in an almost empty groove are significantly reduced.

The ion yield of $(C_{60})_3Et_n$ (Fig. 3) shows a magic number at $n = 2$, probably reflecting the fact that dimple sites on the axis between three fullerenes offer a higher adsorption energy for a single C_2H_4 (~400 meV) than groove or simple hollow sites. In our previous work on $(C_{60})_m(CH_4)_n$ the energetic preference of dimple sites appeared in form of a plateau in the calculated energy at $(E) = 2$ for the C_{60} trimer (and at $(E) = 4$ for the C_{60} tetramer). Fig. 5c shows no such plateau for $(C_{60})_3Et_n$, but investigation using visual molecular dynamics [77] clearly shows that all dimple sites are occupied. Further above we have already speculated on reasons for the absence of plateaus related to the completion of adsorption layers. For dimple sites another possible factor is that they have fewer ethylene neighbors than simple hollow sites. The tetrahedral C_{60} tetramer offers 4 dimple sites but no corresponding feature is seen in the ion yield of $(C_{60})_4Et_n$ nor in the computed (E). Additional work, including calculation of adiabatic adsorption energies, will be needed to elucidate the energetics of dimple sites in C_{60} aggregates for adsorption of C_2H_4.

C_{60} aggregates feature additional magic numbers in the ion yield that we have not yet discussed, namely $n = 28$ for the dimer, and $n = 29$ and 52 for the trimer. The features are broad but they are clearly reproducible. What is their origin? A possible explanation comes from the observation that the numbers are barely smaller than the number of molecules in a complete adsorption layer of the next smaller fullerene aggregate, i.e. $n = 32$ for C_{60} and 55 for $(C_{60})_2$. This suggests a preference of molecules in an incomplete adsorption layer to cover one fullerene at a time once all groove sites are filled. We have tested this model by optimizing C_{60} dimers with 28–32 ethylene molecules initially placed either on one side or equally distributed on both fullerenes in and near the groove. There is a preference for the molecules to cover just one of the fullerenes. The gain in total energy is 78, 175, 171, 166, 154 meV for the dimer with 28, 29, 30, 31, 32 C_2H_4 respectively, with a clear step from 28 to 29, when the first shell is completed on one of the two C_{60} However, with random initial conditions annealing does not result in a configuration where one fullerene is completely covered before Et adsorbs on the other fullerene. Perhaps the effect is underestimated in our simulations because the classical Et–Et interaction is so much (factor 2.81) weaker than the C_{60}–Et interaction. To elucidate these discrepancies, more accurate C_{60}–Et PES calculations that go beyond long-range corrected DFT as well as Et–Et interaction models that go beyond the pair-approximation would be necessary.

5.4. *Orientational order of molecules in the commensurate 1×1 phase and its temperature dependence*

For a highly anisotropic molecule such as C_2H_4 the orientation relative to the substrate is an important parameter. Previous studies of C_2H_4 on graphite have shown that the orientation, and orientational order, depend on coverage x and temperature T [4–8,11–13,15]. As shown in several theoretical studies, isolated molecules prefer to lie flat on the substrate, i.e., with their C=C axis parallel to the substrate ($\alpha = 90°$) and no significant tilt, defined as rotation around the C=C axis, i.e., with $\beta \approx 90°$ (note, however, that we obtained $\beta = 71°$ for a single ethylene on a hexagonal site of C_{60}, see Section 5.2 and Fig. 4). In the low-density (LD) phase, at coverage $x \leqslant 0.83$, α remains near 90° but the interaction between adjacent C_2H_4 may cause significant tilt. In the high-density (HD) phase, when the coverage exceeds $x \geqslant 1.05$, the C=C axis of the molecules will be in a T-shaped configuration ($\alpha = 0°$) thus minimizing their projected size. Mixed phases occur for $0.83 \leqslant x \leqslant 1.05$.

Temperature is another important parameter. Below $T \approx 35$ K the orientation is frozen and molecules form a herringbone pattern on graphite, with an angle of 60° between the C=C axes of adjacent molecules [13,15]. Above 35 K the molecules rotate freely around an axis normal to the surface thus destroying the herringbone pattern. According to an electron diffraction study by Eden and Fain [16,17], the commensurate $\sqrt{3} \times \sqrt{3}$ phase appears at temperatures above 58 K and densities $\approx 0.9 \leqslant x \leqslant \approx 1.03$; the phase melts below 70 K.

We have observed a strong anomaly in the ion yield of $C_{60}Et_n^+$ at $n = 32$ (Fig. 3) which we have attributed to enhanced stability of the commensurate 1×1 phase, the cousin of the $\sqrt{3} \times \sqrt{3}$ phase on planar graphite. The phase becomes accessible for molecules as large as C_2H_4 thanks to the curvature of C_{60}. The 1×1 phase already appeared for several other atoms (He) and molecules (H_2, N_2, O_2, CH_4) but detailed theoretical analysis so far was restricted to complexes containing either helium or CH_4; orientation played no or just a minor role. For C_2H_4 a crucial question relates to the orientation of the molecules in the 1×1 phase, and its temperature dependence.

As discussed in Section 4, the estimated vibrational temperature of $C_{60}Et_{32}$ in the experiment is 110 K. This value is some 60% higher than the temperature at which a submonolayer of ethylene on graphite melts [12,13,16]. However, the enhanced corrugation over the curved surface of C_{60} may significantly increase the melting temperature. We will return to this point at the end of this Section.

Next we analyze the orientational order and its temperature dependence. We have already defined α and β but a third angle is needed to completely characterize the orientation of the molecules. Klein and co-workers used the azimuthal angle ϕ, i.e., the angle between some pre-defined vector in the graphite plane and the projection of the C=C axis onto that plane. The azimuthal angle is not useful for curved surfaces, instead we define an angle γ that measures the mutual orientation between the C=C axis of neighbors [78]. γ will equal 0° (90°) if, in a projected view, the two molecules are parallel (perpendicular). For a herringbone pattern on planar graphite, the distribution of γ would be bimodal with one peak at 0° and another one at ≈60°.

The analysis starts with an annealed and optimized $C_{60}Et_{32}$ aggregate; with a complete first shell and all molecules in hollow sites. The initial structure is heated up 1 K at a time. In each step of the MD simulation an equilibration period of 2 ps is followed by a production run of 2 ps during which the three angles α, β and γ are evaluated. The distributions of α and β *versus* temperature are displayed in Fig. 7; the distribution of γ in Fig. 8. The color scale of the 2D histograms is chosen so that small occupation numbers (white and dark blue) are visible as well as peaks (yellow and red). Each column, representing an interval of 1 K, is normalized with its total sum and the total maximum of all counts.

At lowest temperature only two ethylenes stand vertically ($\alpha = 0°$); the C=C axis of the other 30 molecules lies nearly flat ($\alpha = 85$–$90°$). In contrast, the commensurate $\sqrt{3} \times \sqrt{3}$ phase observed on planar graphite between 58 and 70 K [16] is a high-density phase, i.e., all molecules are vertical ($\alpha = 0°$). With $\beta = 40$–$55°$ the tilt of the molecules on C_{60} is much larger than for a single ethylene over a hexagon ($\beta = 71°$, see Section 5.2). Moller and Klein computed an even larger tilt of $\beta = 35°$ (in our notation). In general the tilt is expected to increase with coverage [15] because it helps to alleviate the problem of crowding (which in our case is substantial, else no molecules would stand vertically). First, the tilt reduces the projected size of the molecules, and second, on the curved surface of C_{60} it increases the radial distance from the center thus increasing the distance between neighboring molecules. The distribution of mutual orientations γ, peaks at 80°; 45% of all molecules lie in the interval $70° \leqslant \gamma \leqslant 90°$, nearly perpendicular to each other. However, there is no second peak in the distribution at 0°, i.e., there is no preference for parallel molecules. Indeed, it is easily seen that it is impossible to form a commensurate phase on the surface of a fullerene that would resemble a herringbone pattern, given that 20 of the 32 molecules in registered sites have 6 nearest neighbors while 12 have 5.

As the temperature increases, ethylene starts to translate and rotate; more and more molecules may escape their strict confinement. The fraction of molecules in the vertical configuration (defined as $\alpha < 50°$) increases gradually from 10.3% at 1 K to 22.5% at 80 K. Klein and coworkers had reported a similar approximately linear increase for ethylene adsorbed on planar graphite [79]. It is worth mentioning that the orientation of individual molecules rarely changes during the duration of a simulation between tangential and vertical if the temperature is below 40–50 K.

The distribution of the tilt angle β initially broadens gradually, but more dramatically at ≈60 K when some molecules start to lie flat ($\beta = 90°$). In their MD study of ethylene on graphite Cheng and Klein also reported a change from a tilted position to flat as temperature increased [13]. On C_{60}, however, even above 60 K tilt angles near 0° are still not populated, i.e., the molecules do not yet rotate freely around the C=C axis.

The transition at 60 K in Fig. 7b should not be confused with the so-called rotator phase [7] in which ethylene on graphite starts to rotate freely around an axis normal to the surface and the molecules form a triangular lattice. That phase appears above 35 K, half the temperature at which the adsorbed layer melts. In the present study the corrugation is much stronger, and the rotator phase would imply a

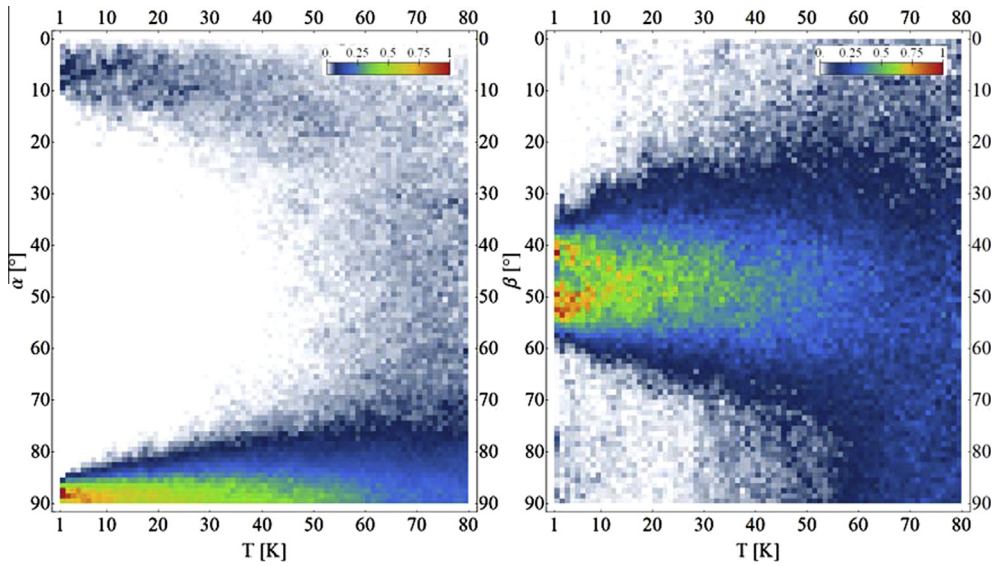

Fig. 7 – Temperature dependence of C_2H_4 orientation for the 1×1 phase on C_{60}. The C=C axis orientation (α, left panel) is measured using the valence angle between the center of mass (COM) of C_{60}, the COM of C_2H_4 and C of C_2H_4. The orientation of the C_2H_4 plane (β, right panel) is measured relative to the plane enclosed by α as dihedral angle (COM-C_{60}, COM-C_2H_4, C, and H). (A colour version of this figure can be viewed online.)

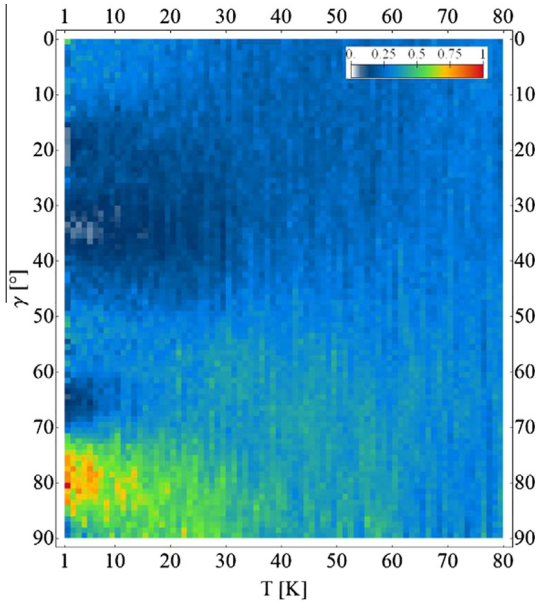

Fig. 8 – Relative orientation of neighboring C_2H_4 molecules for the 1×1 phase on C_{60}. The angle γ measures the orientation between the two C=C axis of two C_2H_4 molecules, corrected for a tilt due to the curvature. γ is produced by projection of the second C=C– axis on the second fullerene face and further projection on the first fullerene face. A detailed definition of γ is given in the text. (A colour version of this figure can be viewed online.)

structureless distribution of γ. Fig. 8 shows no distinct transition for $\gamma(T)$; the change from preferred orientation ($\gamma = 80°$) at low temperature to random orientation appears to occur more gradually between 30 and 60 K.

There are several reasons to expect significant differences in the properties of ethylene adsorbed on graphite, and fullerene. First, as seen in the current work, ethylene on C_{60} strongly prefers to form a commensurate phase because the corrugation is enhanced on convex surfaces [25,26] whereas commensurate phases on graphite escaped detection in all but Eden and Fain's electron diffraction work [16,17]. Commensurate phases on graphite also failed to appear in molecular dynamics simulations [7,79], even when the strength of the corrugation was deliberately increased [13,15]. Second, domain walls play an important role in two-dimensional phase transitions [13]; C_{60} is probably too small to support multiple domains. Third, as shown previously for C_{60}–helium complexes, the number of adsorbed molecules plays a crucial role. The complete layer in $C_{60}Et_{32}$ (i.e., the lack of vacancies) makes it energetically very costly for adsorbate molecules to change sites; they probably would have to be promoted to the second layer for that to happen.

The three arguments presented in the preceding paragraph suggest that in the experiment $C_{60}Et_{32}^{+}$ might be solid even though the estimated temperature, 110 K, is well above the melting temperature of ethylene on graphite. Indeed, there is no reason for $n = 32$ to form a magic number unless the adsorbed molecules form an ordered solid, with all molecules in registered sites. For a molten layer one would expect a magic number once the first adsorption layer is completed. In principle, that could happen at $n = 32$. However, the distribution of the angle α in Fig. 7a shows that the fraction of molecules in vertical position is still small even at 80 K. Therefore additional molecules could still be added to the first layer by changing their orientation, similar to what one observes for the first monolayer on graphite. We conclude that, in the experiment, the 32 ethylene molecules adsorbed on C_{60}^{+} form a commensurate 1×1 layer.

6. Conclusions

We have presented a combined experimental and theoretical study of C_{60}–ethylene complexes. Magic numbers in the experimental ion yield indicate enhanced adsorption energies that occur when specific types of adsorption sites are completely filled; the nature of the sites (registered sites, groove sites, and dimple sites) is identified by comparison with molecular dynamics calculations. Of particular interest is the commensurate phase that forms on the C_{60} monomer when all 32 hollow sites are occupied; on planar graphite commensurate phases are difficult to observe. The curved substrate enhances the corrugation; it also affects the degree of orientational order in $C_{60}(C_2H_4)_{32}$. At low temperature 45% of all nearest-neighbor pairs are perpendicular to each other but there is no second peak in the angular distribution that would indicate anything akin to a herringbone pattern. The distribution of tilt angles shows an abrupt change near 60 K but the mutual orientational order decreases gradually as temperature increases, in contrast to the abrupt transition to a rotator phase that is observed for ethylene on graphite.

Acknowledgements

This work was supported by the Austrian Science Fund, Wien (FWF, projects P19073, P23657, L633, and J2973-N20). Part of this work was supported by the Austrian Ministry of Science BMWF as part of the UniInfrastrukturprogramm of the Research Platform Scientific Computing at the University of Innsbruck and funded by the Austrian Science Fund (FWF) DK+ project Computational Interdisciplinary Modeling, W1227. F.H. acknowledges support from the Tennessee NSF-EPSCoR Grant TN-SCORE (NSF EPS 1004083).

Appendix A. Supplementary data

Supplementary data associated with this article can be found, in the online version, at http://dx.doi.org/10.1016/j.carbon.2013.12.017.

REFERENCES

[1] Steele WA. Monolayers of linear molecules adsorbed on the graphite basal plane: structures and intermolecular interactions. Langmuir 1996;12(1):145–53.
[2] Bruch LW, Diehl RD, Venables JA. Progress in the measurement and modeling of physisorbed layers. Rev Mod Phys 2007;79(4):1381–454.
[3] Steele W. Molecular-interactions for physical adsorption. Chem Rev 1993;93(7):2355–78.
[4] Grier BH, Passell L, Eckert J, Patterson H, Richter D, Rollefson RJ. Neutron-scattering study of ethylene motions on graphite surfaces. Phys Rev Lett 1984;53(8):814–7.
[5] Larese JZ, Rollefson RJ. Rotational transitions in monolayer molecular-solids. Phys Rev B 1985;31(5):3048–50.
[6] Inaba A, Morrison JA. Ethylene on graphite – heats of adsorption and phase-diagram. Phys Rev B 1986;34(5):3238–42.
[7] Klein ML, Morrison JA. Gas surface-potentials and the interpretation of experiments on the ethylene graphite system using molecular-dynamics calculations. Carbon 1987;25(1):23–30.
[8] Larese JZ, Passell L, Ravel B. Orientational ordering of ethylene on graphite. Can J Chem 1988;66(4):633–6.
[9] Mochrie SGJ, Sutton M, Birgeneau RJ, Moncton DE, Horn PM. Multilayer adsorption of ethylene on graphite – layering, prewetting, and wetting. Phys Rev B 1984;30(1):263–73.
[10] Drir M, Nham HS, Hess GB. Multilayer adsorption and wetting – ethylene on graphite. Phys Rev B 1986;33(7):5145–8.
[11] Kim HK, Feng YP, Zhang QM, Chan MHW. Phase-transitions of ethylene on graphite. Phys Rev B 1988;37(7):3511–23.
[12] Larese JZ, Passell L, Heidemann AD, Richter D, Wicksted JP. Melting in 2-dimensions – the ethylene-on-graphite system. Phys Rev Lett 1988;61(4):432–5.
[13] Cheng A, Klein ML. Melting transition of ethylene on graphite. Langmuir 1992;8(11):2798–803.
[14] Barbour AM, Telling MTF, Larese JZ. Investigation of the behavior of ethylene molecular films using high resolution adsorption isotherms and neutron scattering. Langmuir 2010;26(11):8113–21.
[15] Moller MA, Klein ML. The low-temperature structure of ethylene monolayers physisorbed on the graphite basal-plane. Can J Chem 1988;66(4):774–8.
[16] Eden VL, Fain SC. Ethylene on graphite – a low-energy electron-diffraction study. Phys Rev B 1991;43(13):10697–705.
[17] Eden VL, Fain SC. Phase transitions of ethylene monolayers on graphite. J Vac Sci Technol 1992;A10(4):2227–30.
[18] Herrera LF, Do DD, Birkett GR. Histogram of number of particles as an indicator for 2d phase transition in adsorption of gases on graphite. Mol Simul 2010;36(14):1173–81.
[19] Cruz F, Mota JPB. Thermodynamics of adsorption of light alkanes and alkenes in single-walled carbon nanotube bundles. Phys Rev B 2009;79(16):165426.
[20] Esteves IAAC, Cruz FJAL, Muller EA, Agnihotri S, Mota JPB. Determination of the surface area and porosity of carbon nanotube bundles from a Langmuirian analysis of sub- and supercritical adsorption data. Carbon 2009;47(4):948–56.
[21] Cruz FJAL, Esteves IAAC, Mota JPB. Adsorption of light alkanes and alkenes onto single-walled carbon nanotube bundles: Langmuirian analysis and molecular simulations. Colloids Surf A 2010;357(1–3):43–52.
[22] Rawat DS, Migone AD. Ethylene films adsorbed onto purified HiPco single walled carbon nanotubes: a comparison with ethane and longer alkanes. Adsorpt Sci Technol 2011;29(8):723–31.
[23] Albesa AG, Rafti M, Rawat DS, Vicente JL, Migone AD. Ethane/ethylene adsorption on carbon nanotubes: temperature and size effects on separation capacity. Langmuir 2012;28(3):1824–32.
[24] Tascon JMD, Bottani EJ. Ethylene physisorption on C_{60} fullerene. Carbon 2004;42(7):1333–7.
[25] Gordillo MC. ^{4}He adsorbed on the outer surface of carbon nanotube bundles. Phys Rev Lett 2008;101(4):046102.
[26] Gatica SM, Kostov MK, Cole MW. Ordering transition of gases adsorbed on a C_{60} surface: Monte Carlo simulations and lattice-gas models. Phys Rev B 2008;78(20):205417.
[27] Leidlmair C, Wang Y, Bartl P, Schöbel H, Denifl S, Probst M, et al. Structures, energetics and dynamics of helium adsorbed on isolated fullerene ions. Phys Rev Lett 2012;108:076101.
[28] Zöttl S, Kaiser A, Bartl P, Leidlmair C, Mauracher A, Probst M, et al. Methane adsorption on graphitic nanostructures: every molecule counts. J Phys Chem Lett 2012;3(18):2598–603.
[29] Kaiser A, Zöttl S, Bartl P, Leidlmair C, Mauracher A, Probst M, et al. Methane adsorption on aggregates of fullerenes: site-

selective storage capacities and adsorption energies. ChemSusChem 2013;6(7):1235–44.
[30] Kaiser A, Leidlmair C, Bartl P, Zöttl S, Denifl S, Mauracher A, et al. Adsorption of hydrogen on neutral and charged fullerene: experiment and theory. J Chem Phys 2013;138(7):074311.
[31] Echt O, Kaiser A, Zöttl S, Mauracher A, Denifl S, Scheier P. Adsorption of polar and non-polar molecules on isolated cationic C_{60}, C_{70}, and their aggregates. ChemPlusChem 2013;78(9):910–20.
[32] Klots CE. Evaporation from small particles. J Phys Chem 1988;92(21):5864–8.
[33] Klots CE. Kinetic methods for quantifying magic. Z Phys D 1991;21(4):335–42.
[34] Casero R, Soler JM. Onset and evolution of "Magic Numbers" in mass spectra of molecular clusters. J Chem Phys 1991;95(4):2927–35.
[35] Hansen K, Näher U. Evaporation and cluster abundance spectra. Phys Rev A 1999;60(2):1240–50.
[36] Hansen K, Andersson PU, Uggerud E. Activation energies for evaporation from protonated and deprotonated water clusters from mass spectra. J Chem Phys 2009;131(12):124303.
[37] Toennies JP, Vilesov AF. Superfluid helium droplets: a uniquely cold nanomatrix for molecules and molecular complexes. Angew Chemie (Int Ed) 2004;43(20):2622–48.
[38] An der Lan L, Bartl P, Leidlmair C, Schöbel H, Jochum R, Denifl S, et al. The submersion of sodium clusters in helium nanodroplets: Identification of the surface → interior transition. J Chem Phys 2011;135:044309.
[39] Grimme S. Semiempirical gga-type density functional constructed with a long-range dispersion correction. J Comp Chem 2006;27(15):1787–99.
[40] Chai J-D, Head-Gordon M. Long-range corrected hybrid density functionals with damped atom-atom dispersion corrections. Phys Chem Chem Phys 2008;10(44):6615–20.
[41] Ditchfield R, Hehre WJ, Pople JA. Self-consistent molecular-orbital methods. IX. An extended Gaussian-type basis for molecular-orbital studies of organic molecules. J Chem Phys 1971;54(2):724–8.
[42] Hehre WJ, Ditchfield R, Pople JA. Self-consistent molecular orbital methods. XII. Further extensions of Gaussian-type basis sets for use in molecular orbital studies of organic molecules. J Chem Phys 1972;56(5):2257–61.
[43] Klimes J, Michaelides A. Perspective: advances and challenges in treating van der Waals dispersion forces in density functional theory. J Chem Phys 2012;137(12).
[44] Kalugina YN, Cherepanov VN, Buldakov MA, Zvereva-Loete N, Boudon V. Theoretical investigation of the ethylene dimer: interaction energy and dipole moment. J Comp Chem 2012;33(3):319–30.
[45] Pople JA, Head-Gordon M, Raghavachari K. Quadratic configuration-interaction – a general technique for determining electron correlation energies. J Chem Phys 1987;87(10):5968–75.
[46] Dunning Jr TH. Gaussian basis sets for use in correlated molecular calculations. I. The atoms boron through neon and hydrogen. J Chem Phys 1989;90(2):1007–23.
[47] Jorgensen WL, Maxwell DS, Tirado-Rives J. Development and testing of the OPLS all-atom force field on conformational energetics and properties of organic liquids. J Am Chem Soc 1996;118(45):11225–36.
[48] Girifalco LA, Lad RA. Energy of cohesion, compressibility, and the potential energy functions of the graphite system. J Chem Phys 1956;25(4):693–7.
[49] Nosé S. A molecular dynamics method for simulations in the canonical ensemble. Mol Phys 1984;52(2):255–68.
[50] Hoover WG. Canonical dynamics: equilibrium phase-space distributions. Phys Rev A 1985;31(3):1695–7.
[51] Damm W, Frontera A, TiradoRives J, Jorgensen WL. OPLS all-atom force field for carbohydrates. J Comput Chem 1997;18(16):1955–70.
[52] Smith W, Forester TR. Dl_poly_2.0: a general-purpose parallel molecular dynamics simulation package. J Mol Graphics 1996;14(3):136–41.
[53] Unconstrained nonlinear optimization algorithms [accessed 2013 Jul 19]; available from: http://www.mathworks.de/de/help/optim/ug/unconstrained-nonlinear-optimization-algorithms.html.
[54] Kresse G, Furthmüller J. Efficient iterative schemes for ab initio total-energy calculations using a plane-wave basis set. Phys Rev B 1996;54(16):11169–86.
[55] Perdew JP, Burke K, Ernzerhof M. Generalized gradient approximation made simple. Phys Rev Lett 1996;77(18):3865–8.
[56] Blöchl PE. Projector augmented-wave method. Phys Rev B 1994;50(24):17953–79.
[57] NIST Chemistry Webbook [accessed Nov 1, 2013]; available from: http://webbook.nist.gov/chemistry.
[58] Echt O, Sattler K, Recknagel E. Magic numbers for sphere packings: experimental verification in free xenon clusters. Phys Rev Lett 1981;47(16):1121–4.
[59] Kroto HW, Heath JR, O'Brien SC, Curl RF, Smalley RE. C_{60}: buckminsterfullerene. Nature 1985;318:162–3.
[60] Martin TP. Shells of atoms. Phys Rep 1996;273(4):199–241.
[61] An der Lan L, Bartl P, Leidlmair C, Jochum R, Denifl S, Echt O, et al. Solvation of Na+, K+ and their dimers in helium. Chem Eur J 2012;18(14):4411–8.
[62] Klots CE. Temperature of evaporating clusters. Nature 1987;327:222–3.
[63] Shepperson B, Liu J, Ellis AM, Yang S. Ionization of doped helium nanodroplets: residual helium attached to diatomic cations and their clusters. J Phys Chem A 2011;115(25):7010–6.
[64] Andersen JU, Bonderup E, Hansen K. On the concept of temperature for a small isolated system. J Chem Phys 2001;114(15):6518–25.
[65] Branz W, Malinowski N, Enders A, Martin TP. Structural transition in $(C_{60})_n$ clusters. Phys Rev B 2002;66(9):094107.
[66] Tournus F, Charlier JC, Melinon P. Mutual orientation of two C_{60} molecules: an ab initio study. J Chem Phys 2005;122(9):094315.
[67] Zettergren H, Schmidt HT, Reinhed P, Cederquist H, Jensen J, Hvelplund P, et al. Stabilities of multiply charged dimers and clusters of fullerenes. J Chem Phys 2007;126(22):224303.
[68] Doye JPK, Wales DJ, Branz W, Calvo F. Modeling the structure of clusters of C_{60} molecules. Phys Rev B 2001;64(23):235409.
[69] Pacheco JM, Prates Ramalho JP. First-principles determination of the dispersion interaction between fullerenes and their intermolecular potential. Phys Rev Lett 1997;79(20):3873–6.
[70] Takeuchi H. Theoretical investigation on structural properties of ethylene clusters $(C_2H_4)_n$ ($n \leqslant 25$). Comput Theor Chem 2011;970(1–3):48–53.
[71] Chan MC, Block PA, Miller RE. Structure of the ethylene dimer from rotationally resolved near-infrared spectroscopy: a quadruple hydrogen bond. J Chem Phys 1995;102(10):3993–9.
[72] Rezaei M, Michaelian KH, McKellar ARW, Moazzen-Ahmadi N. Infrared spectra of ethylene clusters: $(C_2D_4)_2$ and $(C_2D_4)_3$. Phys Chem Chem Phys 2012;14(23):8415–8.
[73] Bottani EJ. Computer simulation of ethylene physisorption on graphite. Langmuir 1999;15(17):5574–7.
[74] Battezzati L, Pisani C, Ricca F. Equilibrium conformation and surface motion of hydrocarbon molecules physisorbed on graphit. J Chem Soc Faraday Trans 1975;2(71):1629–39.
[75] Tsai C-W, Su Y-C, Li G-D, Chai J-D. Assessment of density functional methods with correct asymptotic behavior. Phys Chem Chem Phys 2013;15(21):8352–61.

[76] Schyman P, Jorgensen WL. Exploring adsorption of water and ions on carbon surfaces using a polarizable force field. J Phys Chem Lett 2013;4(3):468–74.
[77] Humphrey W, Dalke A, Schulten K. VMD: visual molecular dynamics. J Mol Graph 1996;14(1):33–8.
[78] Two problems arise in the definition of an angle γ that measures the relative orientation of neighboring ethylene molecules. First the curvature of C_{60} introduces an average angle that is not of interest. Second the C=C axis are not necessarily parallel to the C_{60} faces. We therefore apply the following double projection: Let R1, R2 denote the centers of mass of two neighboring molecules in hollow sites, and F0 the center-of-mass of C_{60}. The two corresponding fullerene faces are defined by their approximate normal vectors n1 = R1–F0 and n2 = R2–F0. The C=C axis of one molecule (#1) is projected on its own face. This projected vector is normalized and further projected on the plane of molecule #2; this vector is called ppCC1. The C=C axis of molecule #2 is also projected on its face, giving pCC2. Then γ is the angle between ppCC1 and pCC2 that is smaller than 180°.,
[79] Moller MA, Klein ML. The continuous melting transition of ethylene on graphite: a molecular dynamics study. Chem Phys 1989;129(2):235–9.